Nexus : Journal of Innovative Studies of Engineering Science (JISES)
Volume: 02 Issue: 04 | 2023 ISSN: 2751-7578
http://innosci.org/

Influence of Different Two-Phase Velocities on the Simulated Swirling Spray Flame Flows

Alaa Jasim Alshiblawi, Ahmed Abed Al Kadhem Majhool
Mechanical Eng, Eng College, University of Al-Qadisiyah, Iraq

Annotation: The effects of thermal radiation at various swirl levels of primary air flow have been numerically simulated, various velocities (4 m/s, 8 m/s and 16 m/s) as has the combustion of the kerosene fuel spray. used radiation models and the realizable k-model to simulate turbulent quantities. A model with thorough kerosene combustion dynamics is projected using an empirical model with kerosene fuel-specific model parameters. In order to forecast the incident heat flux on the combustor wall and fuel injector, contributions from the gas phase and thermal radiation have been taken into account. The primary flow's swirl has a big impact on the combustor's flow and flame structures. More air is drawn into the flame zone by the higher recirculation at a high swirl, which both shortens the flame and lowers the peak flame temperature while bringing more air to the input plane. As a result, at a high swirl, the radiative heat flow on the peripheral wall diminishes and moves inward toward the inlet plane. However, due to the flame expanding radially, increasing swirl raises the temperature of the combustor wall. The fuel injector is an essential component of the combustor due to the high incident radiant heat flux and high surface temperature. Because of the flame's proximity to the inlet plane, the injector's peak temperature rises as the swirl flow increases. On the other hand, strong swirl conditions near the combustor outlet can result in a more uniform temperature distribution in the exhaust stream. The results of the numerical simulation are compared with the experimental data. The results showed that the swirl angle (40°, 50°, and 60°) and velocity (8 m/s) provided good results through temperature, incidence radiation, turbulent kinetic energy and species.

Key words: P1 radiation model, Spray combustion, Surface to surface, swirl angle, varies velocity.

1. Introduction

Combustors for gas turbines are mostly used in power generation and maritime transportation. The air supplied by the compressor enters the combustor of a gas turbine at numerous points. The primary air is primarily responsible for oxidizing the fuel, the secondary air is utilized to finish the combustion of any leftover species, and the dilution air is responsible for keeping the gas's temperature within metallurgical parameters as it travels through the turbine restrictions. [1]. Through a swirler with either a constant or variable

Nomenclature			
Cp	specific heat (J kg^{-1} K^{-1})	*Greek symbols*	
g_i	gravitational acceleration (m s^{-2})	σ_s	scattering coefficient
k	thermal conductivity (W m^{-1} K^{-1})	σ	Stefan-Boltzmann Constant
p	Static pressure (kg m^{-1} s^{-2})	$\sigma_{S\lambda}$	spectral scattering coefficient
Pr	Prandtl number	a_λ	spectral absorption coefficient
T	Temperature (K)	Φ_v	Rayleigh dissipation function(kg m^{-3})
U_i	velocity (m s^{-1})	μ	molecular viscosity (kg m^{-2}s^{-2})
S_m	mass to gas-phase (kg m^{-3})	$\in$	turbulence dissipation rate
U_p	Droplets velocity (m s^{-1})	G_λ	spectral incident radiation
F_i	momentum force (kg m^{-2} S^{-2})	$S_{G\lambda}$	defined source term
h_i	Enthalpy	λ wavelength	
j_i	diffusion flux (kg m^{-2} S)	α_λ spectral absorption coefficient $I_{b\lambda}$ black body intensity	
r_t	turbulent pranndtl number	*Subscr*	
S_h	volumetric heat source (kg m^{-2} S)	CFD	Computational Fluid Dynamics
S_f	momentum source term (kg m^{-2} S^{-2})	S-to-S	Surface to surface
S_G	Radiation source	RTE	Radiation Transfer Equation
K	turbulent kinetic energy	WSGGM	Weighted Sum Of Gray Gases Model
f	mixture fraction	P1	Spherical Harmonic
		PDF	Probability Density Function

Primary air enters the combustion chamber through the vane angle. When the flow is swirled, the pressure near to the axis decreases and an unfavorable pressure gradient is created, resulting in a central zone of recirculation. By adding a spinning movement to the intake air, the flame length is shortened and the flame's stability is enhanced. Extensive throughout the last few decades. There has been research on the issue of combustion in gas turbines in order to improve the design and performance attributes of the combustors.[2, 3] . Düwel et al. [4]examined ethanol jet flames with a focus on size, velocity, and temperature The dispersed phase's spatial evolution. Mikami et al. [5]counterflow studies spray flames of n-heptane and n-octane poly-dispersed and came to the conclusion that variations in droplet size distribution substantially influenced spray burning behavior, resulting in flames made up of droplets smaller than 50 lm that finally evolved into gas counterflow flames. The distribution of droplet sizes was also determined to have an effect on the extinction limit. Poorhoseini et al. [6]the effect of increasing the quantity of air swirls in liquid fuel burners was investigated. Increased the swirl number lowered NOx emissions and resulted in a lower exhaust temperature from the combustion chamber. Zhou et al. [7, 8] the impact of raising the inlet air swirl number of liquid fuel burners was investigated. It was discovered that increasing the swirl number would lower the exhaust temperature of the combustion chamber and hence reduce nitrogen oxide (NOx) emissions. Finer mesh size turbulence improved evaporation, leading in a longer flame. Zhou et al. [8] the effect of the swirl number on nitrogen oxide production generation was studied, and it was observed that as the swirl number increased, so did the mean flame temperature. The amount of nitrogen oxide emission decreased as the temperature of the exhaust outlet decreased. Bonatesta et al. [9] the effect of the swirl number on exhaust soot concentration was studied, and it was discovered that while the concentration of exhaust soot emissions decreased as the swirl number increased to values greater than 2, the concentration of exhaust soot gradually increased as the swirl number increased to values greater than 2. Patel and Shah.[10] carried performed experimental research to see how different fuel and air velocities alter the appearance of a diffusion flame. Furthermore, they investigated how different vane angles influenced the swirling flow's influence on the length of the flame and discovered that swirling flow makes inverse diffusion flames (IDFs) shorter, wider, and more dependable than (IDFs) without swirling flow. Patel and Shah.[11] the effects of hydrogen enrichment on swirling and non-swirling natural gas diffusion flame conditions were investigated. They discovered that when hydrogen was introduced for a longer period of time, the flame lengthened and the temperature rose in both cases. while the non-swirling flame had a far greater the temperature increases above the whirling flame for a certain mass-based hydrogen addition quantity, accelerating the rate of NOx pollutant generation in the non-swirling scenario. Khelil et al.[12] projected the amount of NOx emitted by a high-whirling Natural gas diffusion flame numerical simulation using the PDF combustion model and the RSM turbulence model. They noticed that in the high-temperature zone, flame formation could be witnessed in the central recirculation zone. Furthermore, this region had the highest rate of NOx creation, whereas low temperatures had the lowest amounts of NOx. The zone of the furnace. Khanafer and Aithal.[13] A numerical analysis was performed to determine how a natural gas diffusion flame's combustion pollutant changes according on the swirl number. Using the commercial FIDAP tool, they did this simulation and concluded that increasing the swirl number significantly enhanced the fuel/air mixing rate and hence lowered Emissions from burning. They discovered that raising the swirl number reduced (CO) and other unburned gases by 3-5 times. Llbas et al.[14] The effect of the swirl number (0-0.8) on the combustion parameters of fuel mixes in a gas-fired combustor was investigated. A coherent combustion model is essential for more exact prediction in reactive modeling. The combustion model PDF/Mixture Fraction was chosen as a consequence because it better captures experimental data and is recommended for mixing fuels. Other mathematical models employed in this study were the P1 radiation model and the k realizable turbulence model of turbulent flow. Methane was utilized as the baseline fuel in the simulations to validate the forecasts. Forecasts and actual experimental results are shown to agree quite well. The combustion parameters of the hydrogen-containing fuel mixes were then modeled using five various swirl numbers ranging from 0 to 0.8 at 0.2 intervals to determine the influence of the swirl number. Changes in the swirl number have a substantial effect on flame temperatures. Because the tangential velocity of the air stream greatly alters the temperature distribution in the combustor. Variations in the swirl number also have an effect on where the higher NOX patches are situated. Jones et al.[15] Large eddy simulations (LES) were used to investigate axial-swirl combustion of kerosene spray, with a particular focus on how evaporating droplets impact flame temperature and species concentrations. The LES-PDF method is used to address both the dispersion (liquid) and gas phases. The liquid phase is described using a Lagrangian formulation, whereas the gas phase is described using an Eulerian technique. The prediction ability of LES with sub-grid size models for spray dispersion and evaporation is investigated, with an emphasis on the impact of unresolved velocity and temperature fields on droplet evaporation rate. The mean velocity fields of the fully linked LES formulation that were observed and those that were simulated accord well. The models accurately depict the whole behavior of spray combustion, including droplet dispersion and evaporation. The enormous velocity changes seen in the shear layer were shown to have a significant influence on the rate of evaporation and, as a result, temperature distributions. The recent study also shown that LES might be utilized to explore the complex flow characteristics of combustion chambers in gas turbines. Yılmaz. [16] the feasible stable laminar flamelet combustion and k. turbulence models were used in this modeling. The amount of hydrogen in the fuel, according to the studies, has a considerable influence on the flame composition. Taking the swirl number into account, the flame of natural gas diffusion was predicted. Hosseini et al. [17]investigated the ANSYS-Fluent CFD code results show impact of inlet air swirl number on (T), radiation heat flux distribution, and dynamic flow behavior in a methane-air diffusion flame. The swirl number was calculated using a special equation using the axial and tangential parts of velocity based on the swirling effect on the conduct of dynamic influx. Applying the (EDM) allowed for the simulation of the chemical reaction (EDM). Furthermore, the P-1 and conventional k- models were used to calculate the Heat flux from radiation and turbulent flow properties. The results showed that developing the internal recirculation zone of the furnace and causing the combustion products to be produced there are both caused by increasing the swirl of incoming air from 0.0 to 0.6. By eliminating the zones with high temperatures, which are the main source of nitrogen oxide production, fuel and air are combined more effectively, enhancing combustion efficiency (NOx). Furthermore, independent of the maximum flame temperature drop, When the swirl number increases, the radial flow distribution and flame heat exchange area both increase. expands. As a result, pollutant NOx is reduced by 58.6 percent and The effectiveness of flux radiation is raised by 36.5%.

Datta and Som. [18] investigate the effects A computer model based on stochastic separated flow analysis of typical diffusion-controlled spray combustion of liquid fuel in a gas turbine combustor examines the effects of combustor pressure and input swirl on the combustion and emission characteristics within the combustor. was developed. Increased swirl number reduces NOx emissions while enhancing pattern factor at all combustor pressures, according to research. However, whereas an increase in swirl number reduces combustion efficiency at low pressure, it has the reverse effect at high pressure. As pressure rises, the pattern factor improves, while combustion efficiency falls and NOx emissions rise. Rohani and Saqr. [19] are looking at the effect of hydrogen on the temperature and pollutant emissions of a chaotic, unconfined, spinning methane/air flame. The attainable k- combustion and turbulence models, as well as the constant laminar flamelet, were employed. The probability density function was used. There is a substantial variance in the quantity of hydrogen in the fuel stream between 0 and 50% of the fuel volume flow rate. The results show that the flare structure varies dramatically as the volumetric hydrogen proportion in the fuel stream increases. Peak temperature rises when the area of maximum temperature reduces to a tiny region near the flame tip, increasing NO emission levels. The flame containing 10% hydrogen appears to match the conventional pattern very somewhat. Given that the amount of hydrogen consumed is insufficient to affect the combustion parameters of the flame, this is thought to be the result of a change in flow field caused by a change in fuel density.

Joung and Huh. [20] the basic swirling commercial methane-fueled gas turbine combustor and flames were explored, and promising experimental results encapsulating the turbulence-chemistry relationship were revealed. Choi and Baek. [21] radiation shorter droplet trajectories result from enhanced spray combustor performance, which increases the amount of the high-temperature region within the combustion chamber.

the first goal of this study is to examine the influence of swirl number on flame structure and emission parameters in a coaxial burner. In this regard, the emergence and emissions of the flameCO2 and NOx are evaluated using the swirled with a vane. Angle of 40°, 50°, and 60°. The impact of the radiation models and swirling flow on thermal efficiency and emission are examined.

2. Methodology

2.1. Liquid phase

It has been proposed that the liquid phase (discrete droplets) in the gas phase (continuous phase) is spherical. The model determines the trajectory of liquid-phase droplets at the onset of solutions by integrating the force balance with the Lagrangian approach. The following issue is solved for the liquid phase using the governing equations presented in[22] , which have been updated and altered following the computation and modification of the gas phase.

$$\frac{du_p}{dt} = f_D\left(u - u_p\right) + \frac{g_{x(\rho_p - \rho)}}{\rho_p} + \frac{\rho}{\rho_p} u_p \frac{\partial u}{\partial x_i} \qquad (1)$$

$$f_D = \frac{18\mu}{\rho_p d_p^2}\frac{c_D R_e}{24} \qquad (2)$$

$$R_e = \frac{d_p \rho |u_p - u|}{\mu} \qquad (3)$$

Where the droplets velocity is u_p in (m/s), the drag force effect per unit particle mass is $f_D(u - u_p)$ in ($m\ /s^2$), the gravitational force effect on the droplet is ($\frac{g_{x(\rho_p-\rho)}}{\rho_p}$). The third term is an extra force on the right hand. created by the difference in pressure between the fluid. $\frac{du_p}{dt}$ Term denotes the evaporation rate of the particle. The gravity is g_x in ($m\ /s^2$), the droplet diameter is d_p, and the drag coefficient is C_D, and a_1, a_2, anda_3 can be defined as constants given by[23] . Heat transfer between the gaseous and liquid phases is determined by the heat balance. One of the most important things is to investigate the effect of the particles' drag force. Drag correlation Morse and Alexander [23] is used to characterize the drag force coefficient (CD), assuming that the droplet has a spherical form.

$$CD = a_1 + \frac{a_2}{R_e} + \frac{a_3}{R_e^2} \qquad (4)$$

Where:$a_1 . a_2 . and\ a_3$ are constants. The differential in the concentration of vapor between the gas phase and the droplet surface influences the rate of vaporization. The term of the volumetric source denoted by $S_h is$ can be expressed as follows:

$$S_h = \left[\frac{\bar{m}_p}{m_{p.o}} cp\Delta T_p + \frac{\Delta m_p}{m_{p.o}}\left(-h_{fg} + \int_{T_{ref}}^{T_p} C_{p.i} dt\right)\right]\dot{m}_{p.o} \qquad (5)$$

To solve the two interrelated stages, iterative strategies are used. After estimating a particle path, the particle's mass, heat, and momentum acquired or lost in the stream are determined. The mass transfer from the liquid phase to the solid phase is subsequently taken into account in the calculations for the gas phase. The mass fluctuations between the control volumes are utilized to compute gas-phase S_m. It is calculated using the following equations:

$$S_m = \frac{\Delta m_p \dot{m}_{p.o}}{m_{p.o}} \qquad (6)$$

Where the particle mass change in each control volume is Δm_p, the initial mass flow rate of the particles is $m_{p.o}$, and the mass flow rate of particles is m_p. The exchanging mass is then used as a source of mass in the gas-phase and species equation's continuity equation. The change in a particle's momentum across control volumes may be used to represent the momentum transfer between two phases using:

$$F_i = \sum\left(\frac{18\mu}{\rho_p d_p^2}\frac{c_D R_e}{24}(u - u_p) + \frac{g_{x(\rho_p-\rho)}}{\rho_p} + \frac{\rho}{\rho_p} u_p \frac{\partial u}{\partial x_i}\right)\dot{m}_p \Delta t \qquad (7)$$

2.2. Gas-Phase

The Eulerian multiphase is controlled by the equations for continuity, momentum, and energy conservation. Each phase is addressed independently, and the gas phase is represented as a continuum. Each phase of the system is subjected to the mass conservation equation. The model only considers the gas phase when a process begins, not the interaction of two phases. The source term is derived once the paths of the particles are solved. The gas phase is resolved in Fluent Ansys by include the source term in the equation.

$$\frac{\partial}{\partial x_i}(\rho ui) = \boldsymbol{S_m} \qquad (8)$$

Where in gas-phase, the air velocity is u_i in $({}^{m}/_{s})$, The liquid phase's mass addition from the gas phase is S_m in $(kg/m^3 s)$.

Momentum:

$$\rho u_i \frac{\partial ui}{\partial xi} = \frac{\partial}{\partial xj}\left[\mu\left(\frac{\partial ui}{\partial xj} + \frac{\partial uj}{\partial xi}\right) - \frac{2}{3}\mu(\frac{\partial uj}{\partial xj})\delta ij\right] + \rho gi - \frac{\partial p}{\partial xi} + Fi \qquad (9)$$

Where the momentum source term is Fi in $(kg/m^2 s^2)$, the gravity is gi in (m/s^2), a molecular viscosity μ is in $((kg/m^2 s^2)$,

Energy:

$$\rho ui \frac{\partial e}{\partial xi} = -p\frac{\partial ui}{\partial xi} + \Phi v + \frac{\partial}{\partial xi}\left(k\frac{\partial T}{\partial xi}\right) + \frac{\partial}{\partial xi}(\sum_{i=1}^{n} h_i J_i) + S_n \qquad (10)$$

the static pressure is P in (pa), and the equation inclusion species diffusion and the exchange energy source between gas-phase and liquid-phase, the s_n volumetric heat source, estimates the heat transfer utilizing: where the internal energy is e in (J/kg) , the Rayleigh dissipation function is Φv in $(kg/S^2 m)$, the thermal conductivity is K in (W/mk)), the enthalpy of species i is h_i, the temperature of the air is T in (k). A species' diffusion flow is (J_j), and the volumetric heat source is Sn in $(kg/S^2 m)$. The equations for species conservation that forecast the local mass fraction of every species, gas-phase of liquid fuel and air, are:

$$\rho ui \frac{\partial mi}{\partial xi} = -p\frac{\partial J_i}{\partial x_i} + S_m \qquad (11)$$

$$J_i == -\rho D_{i,m}\frac{\partial m_i}{\partial x_i} \qquad (12)$$

Where the local mass fraction of species i is m_i , and the diffusion coefficient for species I in the mixture $D_{i.m}$.

2.3. Turbulence modelling

Turbulent flow is a mathematical model of turbulence used in practical and industrial applications. The turbulence model was used to anticipate turbulence changes using simple equations.

2.3.1. Standard k- ϵ modelling

The derivation of the Standard model excludes the effects of molecular viscosity and assumes that the flow is completely turbulent. It is only ideal for extremely turbulent conditions. According to their relative turbulence dissipation rates ϵ and turbulent kinetic energy values k:

$$\frac{\partial}{\partial t}(\rho k) + \frac{\partial}{\partial x_i}(\rho k u_i) = \frac{\partial}{\partial x_j}\left[(\mu + \frac{\mu_t}{\sigma_k})\frac{\partial k}{\partial x_j}\right] + G_k + G_b - \rho\epsilon - Y_m + S_k \qquad (13)$$

$$\frac{\partial}{\partial t}\rho\epsilon + \frac{\partial}{\partial x_i}(\rho \in u_i) = \frac{\partial}{\partial x_j}\left[(\mu + \frac{\mu_t}{\sigma_\epsilon})\frac{\partial \epsilon}{\partial x_j}\right] + C_{1\epsilon}\frac{\epsilon}{k}(G_k + C_{3\epsilon}G_b) - C_{2\epsilon}\rho\frac{\epsilon^2}{k} + S_\epsilon \qquad (14)$$

$$\mu_t = \rho C_m \frac{k^2}{\epsilon}, \qquad G_k = -\rho u'_i u'_j \frac{\partial u_j}{\partial x_i}, \qquad G_b = \beta g_i \frac{\mu_t \partial T}{Pr_t \partial x_i}$$

Where: The Turbulent viscosity is μ_t, the effect of buoyancy is G_b the Rate of dissemination is Y_m, turbulent kinetic energy generation is G_k, and the Turbulent velocity is u', the coefficient of the thermal expansion is β is the turbulent Prandtl number is Pr_t is at default =0.85, the sours terms defined by used are S_k, S_ϵ and the reverse active prandtle are σ_ϵ, σ_k for $\epsilon.K$ respectively. Constants model at default value is: $C_{1\epsilon}$ =1.44, $C_{2\epsilon}$=1.92, C_m =0.09, σ_k =1, σ_ϵ =1.3, $\sigma_{3\epsilon}$ =-0.33.

2.4. Combustion model

In this work, the probability density function (pdf) was utilized to evaluate a few combustion parameters. A clipped Gaussian and a beta function are two types of probability density functions that may be generated from the mixture fraction to demonstrate how much of the conserved scalar is affected by turbulence fluctuation. Because of its simplicity and low cost, a beta function is commonly used in the present study. The beta function's mathematical identification:

$$p(f) = \frac{f^{\psi-1}(1-f)^{B-1}}{\int_0^1 f^{\psi-1}(1-f)^{B-1}df} \qquad (15)$$

$$f = \frac{z_i - z_{i,ox}}{z_{i,fuel} - z_{i,ox}} \qquad (16)$$

Where the coefficients Ψ and B are representing the explicit functions of the mass average mixture fraction (f̆) as well as the concentration fluctuation (g), described by

$$\psi = \tilde{f}\left[\frac{\tilde{f}(1-\tilde{f})}{g} - 1\right] \qquad (17)$$

B=(1-$\hat{f}$)ψ (18)

When the$\breve{f}$ and g are determined from the Finite Difference solutions at each grid point, the species concentration mean values, product temperature, density, and enthalpy are determined by weighting theses quantities with pre-assumed Probability Density Functions of the mixture fraction,$\breve{p}$ (f) might be adequately specified. The Favre-averaging quantity$\breve{Q}$ can be determined from the quantities of each $y_i(f)$, $H_i(f)$, T(f), and$\rho(f)$ are representing the instantaneous of the mixture fraction (f).

$$\tilde{Q} = \int_0^1 \breve{p}\,(f)Q(f)df \qquad (19)$$

After determining Ψ and p from the defined values of $\hat{f}$ and g using both (17) and (18) equations, additionally, Beta PDF depends only on the Mixture Fraction. Appropriate number for example N=100 of separate amounts of $Y_i(f)$, T(f), etc., were accounted from the state equations for mixture fraction in the domain (0-1) and stocked in tabular formulating.

2.5. Radiation

2.5.1. The P-1 Radiation Modelling

The P-1 radiation model is a condensed variant of the P-N model in which I is extended into an orthogonal series of spherical harmonics.[24] [25]. The equations utilized in the P-1 model are detailed in this section. See Using the Radiation Models for details on how to set up the model. The P-1 radiation model is the most basic version of the P-N model. If just four terms in the series are used to approximate gray radiation, the radiation flow is given by the following equation:

$$q_r = \frac{1}{3(a+\sigma_s)-C\sigma_s} \nabla G \qquad (20)$$

Where the absorption coefficient is α, the scattering coefficient is σs, the incoming radiation is G, and the linear-anisotropic phase function coefficient is C. Following the parameter's introduction.

$$\Gamma = \frac{1}{(3(a+\sigma_s)-C\sigma_s)} \qquad (21)$$

Equation (23) simplifies to

$$q_r = -\Gamma\nabla G \qquad (22)$$

The transport formula for G is

$$\nabla.(\Gamma\nabla G) - a\,G + 4an^2\sigma\,T^4 = S_G \qquad (23)$$

Where σ is the Stefan-Boltzmann constant, n is the medium's refractive index, and SG is a radiation source that is defined by the user. The equation is solved by ANSYS Fluent to produce the incident radiation. When the P-1 model is in operation. Formula Combination (17) and Equation (18) yields the following equation:

$$-\nabla.q_r = aG - 4an^2\,\sigma T^4 \qquad (24)$$

The expression for - ∇. q_r may be used to directly account for heat sources in the energy equation (or sinks) induced by radiation. To mimic non-gray radiation with a gray-band model, Equation (18) is modified as follows:

$$\nabla.(\Gamma_\lambda\nabla G_\lambda) - a_\lambda G_\lambda + 4a_\lambda n^2\sigma T^4 = s_{g\lambda} \qquad (25)$$

Where n is the medium's refractive index, aλ is the spectral absorption coefficient, and G_λ is the spectrum of incident radiation, $S_{G\lambda}$ is a user-defined source term. Γ_λ is defined as:

$$\Gamma_\lambda = \frac{1}{(3(a_{\lambda}+\sigma_{s\lambda})-C\sigma_{s\lambda})} \qquad (26)$$

Where C is the coefficient of the anisotropic linear phase function and ($\sigma_{s\lambda}$)is a spectrum scattering coefficient. Black body spectral emission ($G_{b\lambda}$) between wavelength λ1 and λ2.

$$G_{b\lambda} = 4[F(0\rightarrow n\lambda_2T) - F(0\rightarrow n\lambda_1T)]\sigma T^4 \qquad (27)$$

Where $F0 \rightarrow n\lambda$ is the portion of radiant energy that a black body emits in the wavelength range. The wavelength boundaries of the band are λ_1 and λ_2, and it ranges from 0 to λ at temperature T in a medium with refractive index n. The following formula is used to calculate the spectral radiative flux: 2T

$$q_\lambda = -\Gamma\nabla G_\lambda \qquad (28)$$

The energy equation's radiation source term is expressed as

$$-\nabla q_r = \sum_{AllBands} -\nabla q_{r,\lambda} = \sum_{allBands} a_\lambda(G_\lambda\text{-}n^2G_{b\lambda}) \qquad (29)$$

2.5.2. The Surface to surface Model Equations

Directly emitted and reflected energy make up the energy flux leaving a particular surface. The incident energy flux from the surroundings determines the reflected energy flux, which may then be represented in terms of the energy flow leaving all other surfaces. The energy emitted by the surface k is

$$q_{out,k} = \varepsilon_k\sigma T_k^4 + \rho_k q_{in,k} \qquad (30)$$

where $q_{out,k}$is the energy flux leaving the surface, ε_k is the emissivity, σ is the Stefan-Boltzmann constant, and $q_{in,k}$ is the energy flux incident on the surface from the surroundings.

The amount of incident energy upon a surface from another surface is a direct function of the surface- to-surface “view factor, F_{jk}. The view factor, F_{jk} is the fraction of energy leaving surface j that is incident on surface k. The surfaces used in the calculation of a view factor can be mesh faces or (for 3D cases only) clusters of faces. The incident energy flux $q_{in,k}$ can be expressed in terms of the energy flux leaving all other surfaces as

$$A_k q_{in,k} = \sum_{j=1}^{N} Aj\,q_{out,j}\,F_{jk} \qquad (31)$$

where A_k is the area of surface k and F_{jk} is the view factor between surface k and surface j. For N surfaces, using the view factor reciprocity relationship gives.

so that

$$q_{in,k} = \sum_{j=1}^{N} F_{kj}\, j q_{out,j} \qquad (32)$$

Therefore,

$$q_{out,k} = \varepsilon_k \sigma T_k^4 \rho_k \sum_{j=1}^{N} F_{kj}\, j q_{out,j} \qquad (33)$$

which can be written as

$$J_k = E_k + \rho_k \sum_{j=1}^{N} F_{kj} J_j \qquad (34)$$

where J_k represents the energy that is given off (or radiosity) of surface k, and E_k represents the emissive power of surface k.

3. Numerical method, operating parameters and boundary conditions

Ansys Fluent 19.0 is used to solve all of the governing equations. Three-dimensional geometry in the Cartesian coordinate system has been solved using the pressure-based stable solver. The SIMPLE algorithm was used to carry out the coupling between pressure and velocity. Power law is used to discretize the variables in the momentum and mixture fraction equations. Second order up winding the solution, an unstructured approach, whereas the energy equation is discretized using this scheme. Simulations in the discrete phase and continuous gas phase have been carried out.300 continuous phase iterations are taken into account for each discrete phase iteration when iterating. Twenty in the simulation the test conditions of kerosene/air spray are mentioned in table (1).

Table (1) Numerical test conditions [26]

Fuel conditions		Units
Injector inlet and ambient temperature	300	k
Injector diameter	0.25	mm
Air initial velocity	8.66	m/s
Fuel initial velocity	28	m/s
Injector's flow rate	3.6×10^{-4}	Kg s^{-1}
Mass flow rate of air	0.04	kg s^{-1}
Injection pressure	6	bar

Just before the combustor zone, a swirled is installed in the primary air stream (Figure 1). In this study, three distinct swirled vane angles of 40°, 50°, and 60° were used to examine the impact of degree of swirl on key combustion characteristics. The relation [26] is used to compute the swirl number.

$$SN = \frac{2}{3} \frac{(D_s^3 - D_h^3)}{(D_s^2 - D_h^2)(D_s - D_h)} \tan\theta \qquad (35)$$

Where, as shown in Figure 1, Ds is the swirler's outer diameter, D_h is its hub diameter, and is the vane angle. The turbulence intensity is set at 4% for both the primary and secondary intake, and the length scale is 0.007 m. Based on the maximum value of the mixing length in the combustor duct [26], the length scale was selected. The outlet boundary's pressure outlet boundary condition has been chosen. Stainless steel is the only material that has been specified for the walls. A mixed (convection and radiation) boundary condition has been specified to account for the heat loss from the system to the atmosphere, with the walls being assumed to be non-slip. Along with the exterior and internal emissivity of the material used to make the wall surface, a computed value for the heat transfer coefficient between the outer wall and the atmosphere has also been provided. The ambient temperature is set at 300 K, and the wall's thickness is assumed to be 5 mm. The fuel injector wall, however, is thought to be adiabatic. All of the walls are designated as reflecting walls for DPM calculations. Figure 2. Depicts the two-dimensional structural grid's computational domain. The region adaption strategy is used in this research. It is appropriate for a specific solution domain region. A two-dimensional inside improvement of the quadrilateral is examined. The standard case, which delivers the best numerical simulation to the experimental data when compared without mesh, is reached after two cycles of adaption. The number of mesh has affected numerical results, as seen in figure 3. As a result, three adoptions are employed. Using initial adaption (20800,42052,21253), some numerical results were obtained. As a second adaption, a higher mesh density (83200,167304,84105) is used in the next step. The outcome in this example differs from the initial adaption. The final adaption (83200,167304,84105) is then achieved by using a higher cell density. All numerical values obtained using the third adaption are comparable to those obtained using the second adaption. The numerous mesh generators create meshes with cell volumes that increase quickly as they get farther away from boundaries. While this naturally prevents a mesh from becoming too dense, it can become problematic if the mesh is not fine enough to stop the flow. Region adaptation can be used to refine the mesh if a finer mesh is required in a particular area of a solution domain. For places that demand high resolution, region adaption is particularly crucial. Two-dimension is used in this work. The computational domain employed in two situations is depicted in Figure (2). The results from the three levels of grid resolution are various in the three levels: coarse, medium, and fine. The best results show in the third level (fine grid).

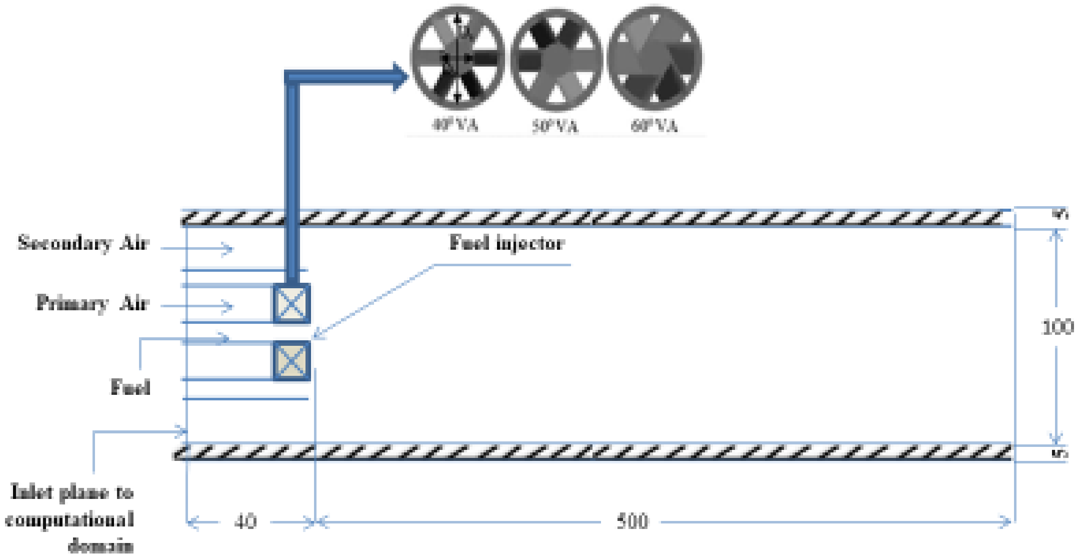

Figure 1. Schematic of the model combustor along with the swirlers with different vane angles.

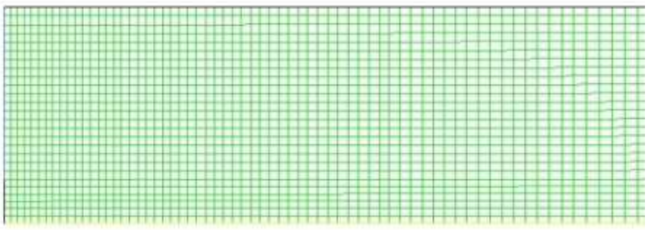

a. Coarse mesh

B-Medium mesh

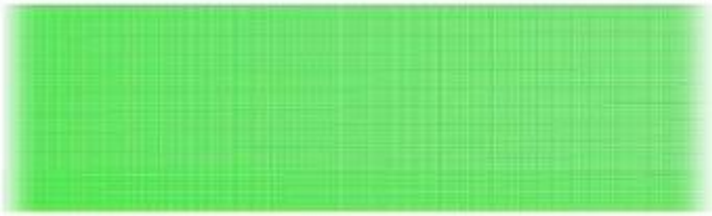

C. Refine mesh

Figure 2. The computational domain. Numerical values obtained using the third adaption are comparable to those obtained using the second adaption

Table (2). The grid specification [27]

Details	Coarse mesh	Medium mesh	Refine mesh
CELL	5200	20800	83200
Faces	10626	42052	167304
Nodes	5427	21253	84105

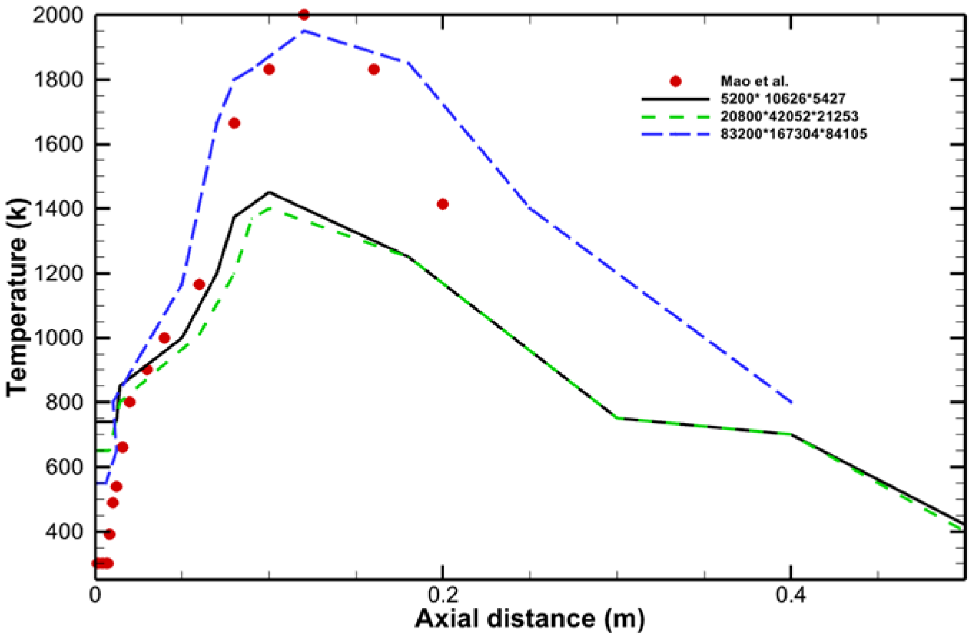

Figure 3. Comparison between the adaption effects of prediction gas temperature with experimental data.

4. Results and discussion

The numerical model's validation has been carried out, and our goal is to determine the turbulence-chemical interaction using the significantly reduced chemistry used in the current model by comparing the agreement between the present prediction and the Ghose et al. The two-phase interactions between the gas and droplet phases haven't been included in this first phase of validation, though, because the fuel is thought of as pre-vaporized kerosene Figure (4) shows the midline temperature change in a turbulent kerosene vapor-air diffusion flame based on measurements, current predictions, and the injection conditions of spray droplets, taken from Ghose et al. Figure 4. shows a comparison between the temperature for the three velocities against the Ghose et al around swirl angle 40◦. These profiles are reaching maximum values near the nozzle region due to

hydrodynamic and chemical reaction between two phases. It can be noticed that the velocity 8 m/s has a very close trend compared with Ghose et al. The difference between the experimental data and numerical simulation is recording as 1.5% of the velocity 8 m/s results, 2.4% of the velocity 4 m/s, and 3 for velocity 16 m/s. At a velocity of 4 m/s, the highest temperature 1830 k around 0.002m from the combustor inlet plane less then 800k around 0.1m, at a velocity of 8 m/s, the highest temperature 1990 k around 0.1m less then 700k around 0.5m. There is a drop in temperature after attaining the highest value, along the axial direction. At a velocity of 16 m/s, the highest temperature 2200 k around 0.001m less then 1000k around 0.5m.

Figure 5. shows a comparison between the temperature for the three velocities against the Ghose et al around swirl angle50◦. These profiles are reaching maximum values near the nozzle region due to hydrodynamic and chemical reaction between two phases. It can be noticed that the velocity 8 m/s has a very close trend compared with Ghose et. The difference between the experimental data and numerical simulation is recording as 1.6% of the velocity 8 m/s results, 2.4% of the velocity 4 m/s, and 3 for velocity 16 m/s. At a velocity of 4 m/s, the highest temperature 1600 k around 0.001m from the combustor inlet plane less then 1300k around 0.06m, at a velocity of 8 m/s, the highest temperature 2200 k around 0.1m less than 800 k around 0.5m There is a drop in temperature after attaining the highest value, along the axial direction. At a velocity of 16 m/s, the highest temperature 2500 k around 0.001m, Then the temperature decreases to 1800 K at 0.5m

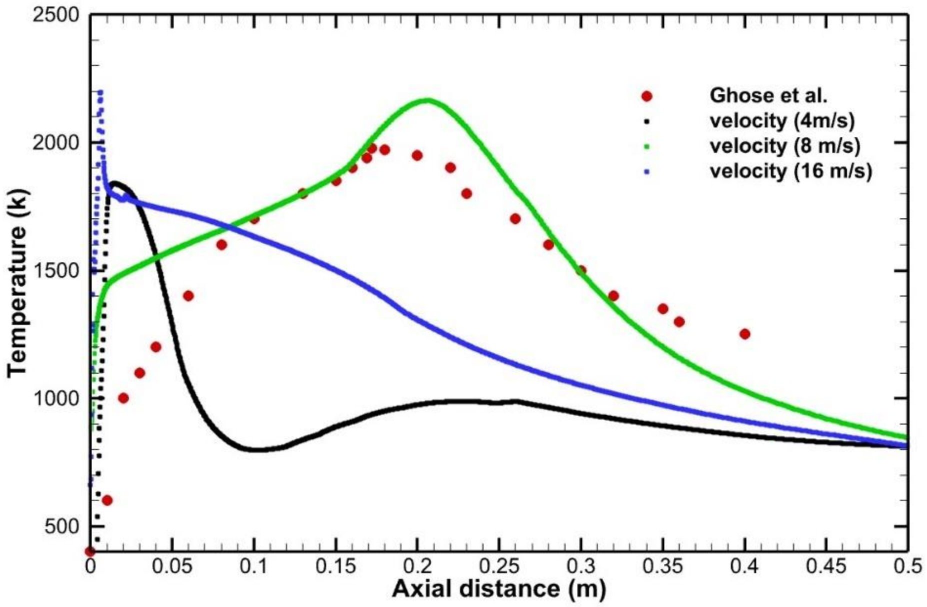

Figure 4. Comparison between at different velocity (4 m/s, 8 m/s, 16 m/s) for temperature variation on the central vertical combustor plane along with superimposed velocity vectors at different swirler vane angles 40°

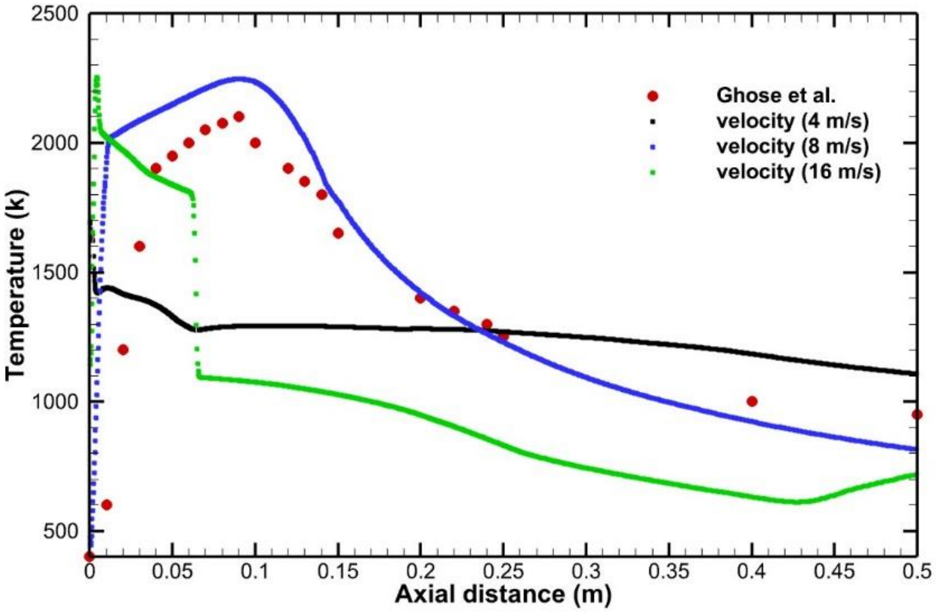

Figure 5. Comparison between at different velocity (4 m/s, 8 m/s, 16 m/s) for temperature variation on the central vertical combustor plane along with superimposed velocity vectors at different swirler vane angles 50°

Table 3. Swirler vane angles are used in simulations.

case	Vane angle(°)	Swirl number
A	40	1.038
B	50	1.474
C	60	2.142

Velocity and temperature distributions

Figures 6(a)–(c) depict the temperature contours in vertical planes across the combustor axis, as well as the corresponding velocity vectors, for the three swirl scenarios (Table 3). The high-temperature zone that forms in the combustor can be used to represent the flame region. It is clear from the figures that the flame in the combustion chamber is relatively long for the primary air case with a modest swirl (Case A), however, as the swirl strength increases, the flame gets smaller and smaller. The primary flow enters tangentially surrounding the axis of the combustor, and a central toroidal recirculation zone is formed. In Case A,

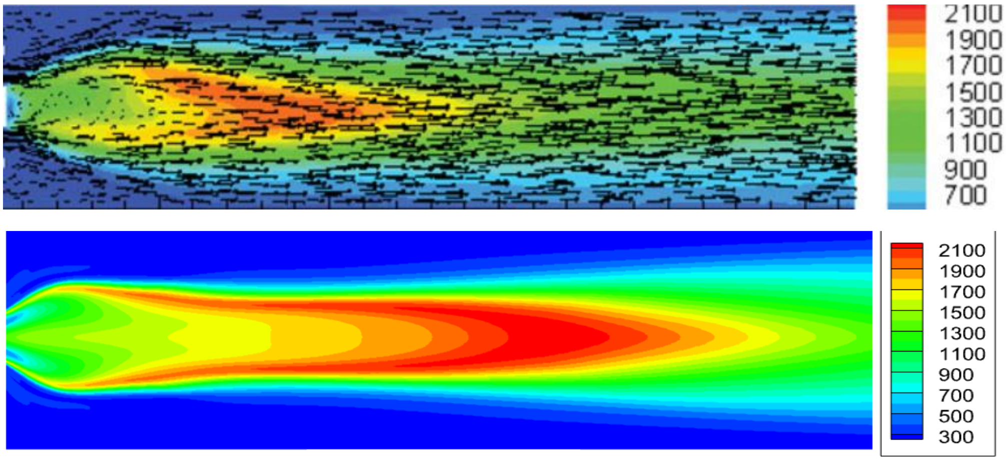

(a)

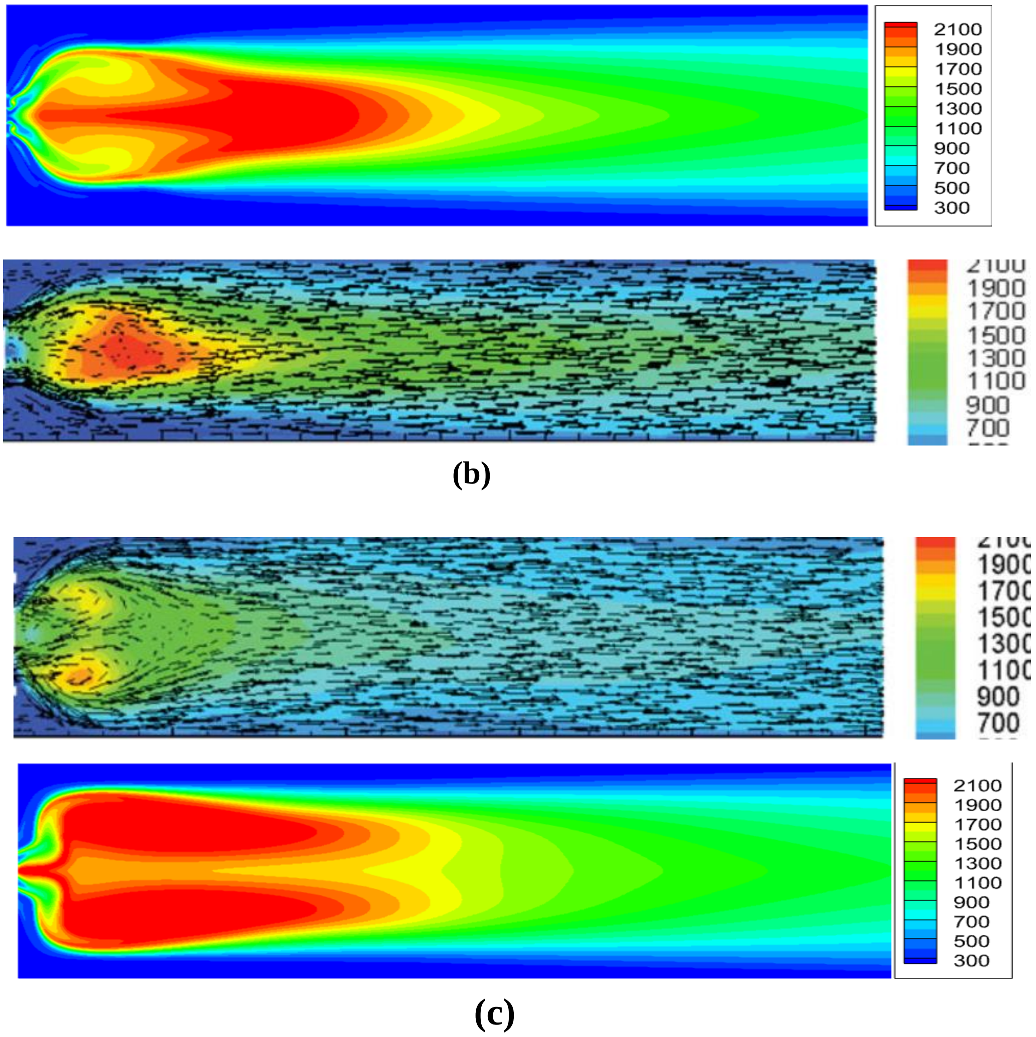

Figure 6. Temperature variation on the central vertical combustor plane along with superimposed velocity vectors at different swirler vane angles: (a) 40° (Case A); (b) 50° (Case B); (c) 60° (Case C)

Due to the low swirl number at flow entry, the recirculation zone's strength is quite low. The fuel that was injected evaporates, combines with air, and travels axially ahead to burn around the center axis under the influence of flow. Because of this, the zone with the maximum temperature is on-axis, and the flame develops downstream of the center on-axis vortex. In this instance,

1. the peak temperature is estimated to be 1988 K and is situated 0.18 m from the combustor's inlet plane.
2. The central recirculation gets stronger when the inlet swirl number is raised to 1.474 (Case B). The fuel-air combination is concentrated closer to the inlet than before thanks to the powerful recirculating bubble. The maximum temperature contours, which reflect the flame zone, continue to be on the axis but migrate closer to the entrance (Figure 6(b)).
3. The maximum temperature (2060 K. Due to more vigorous burning than at 0.08 m from the combustor inlet), the prior instance.
4. The reverse flow is considered in Case C for the maximum swirl number. Recirculation becomes so powerful that it draws gas from a downstream area and quickly transports it upstream (see Figure 6(c)). The flame is split by the powerful reverse flow. Off-axis forces cause it to shift. Consequently, the flame takes on an annular shape and spreads throughout the

radial motion. Moreover, the recirculation bubble's powerful vertical patterns provided considerable flow turbulence. The peak temperature drops to 1862 K as a result of the turbulence, which occurs at a radial location of 0.02 m below the combustor axis and at an axial distance of 0.05 m from the combustor inlet plane. The structure of flame structure is illustrated by the temperature dispersion along the combustor centerline.

Species mass fraction distribution along the axis

Species mass fraction distribution along the axis the distribution of several important species along the center region is depicted in Figures (7, 8 and 9). As shown in various velocity, the combustor's axis for species. The proportion of plotting species (indicated on the secondary axis) identifies the reaction in the pictures. Zone on the centerline of the compressor.

1. The fuel (C12H23) vapor in the velocity 8 m/s closer to Ghose et al case According to Figure 7 (a), the mass fraction at the injector is 0.7. At about 0.001 m from the injector plane, the fuel vapor concentration rapidly to become less than 0.15 around 0.03 m, the fuel vapor concentration rapidly increase around velocity 4 m/s, decreases at velocity 16 m/s. The co2 mass fraction in the velocity 8 m/s closer to Ghose et al case According to

2. Figure 7 (b), the mass fraction at the injector is 0.06. At about 0.001 m from the injector plane, the co2 mass fraction concentration rapidly to become more than 0.15 around 0.23 m, the co2 mass fraction concentration velocity 4 m/s and 16 m/s increase 0.12 around 0.002m then decrease 0.05 around 0.5m. The H2O mass fraction in the velocity 8 m/s closer to Ghose et al case According to

3. Figure 7 (c), the mass fraction near injector is 0.08 about 0.001 m from the injector plane, the H2O mass fraction concentration to become less than 0.05 around 0. 3 m, the H2O mass fraction concentration decreases around velocity 4 m/s and 16 m/s. The N2 mass fraction in the velocity 8 m/s closer to Ghose et al.

4. Figure 7 (d), the mass fraction near injector is 0.08 about 0.001 m from the injector plane, the N2 mass fraction concentration to become less than 0.05 around 0. 3 m, the N2 mass fraction concentration decreases around velocity 4 m/s and 16 m/s. The O2 mass fraction in the velocity 8 m/s closer to Ghose et al.

5. Figure 7 (e), the mass fraction at the injector is 0.001. At about 0.001 m from the injector plane, the O2 mass fraction concentration rapidly to become more than 0.1 around 0. 3 m, the O2 mass fraction concentration rapidly increases around velocity 4 m/s and 16 m/s.

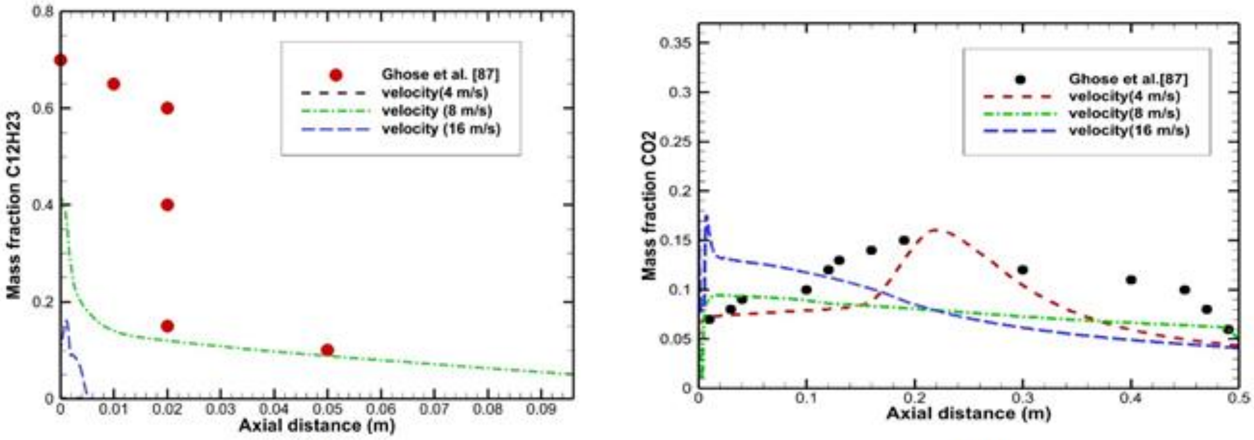

(a) (b)

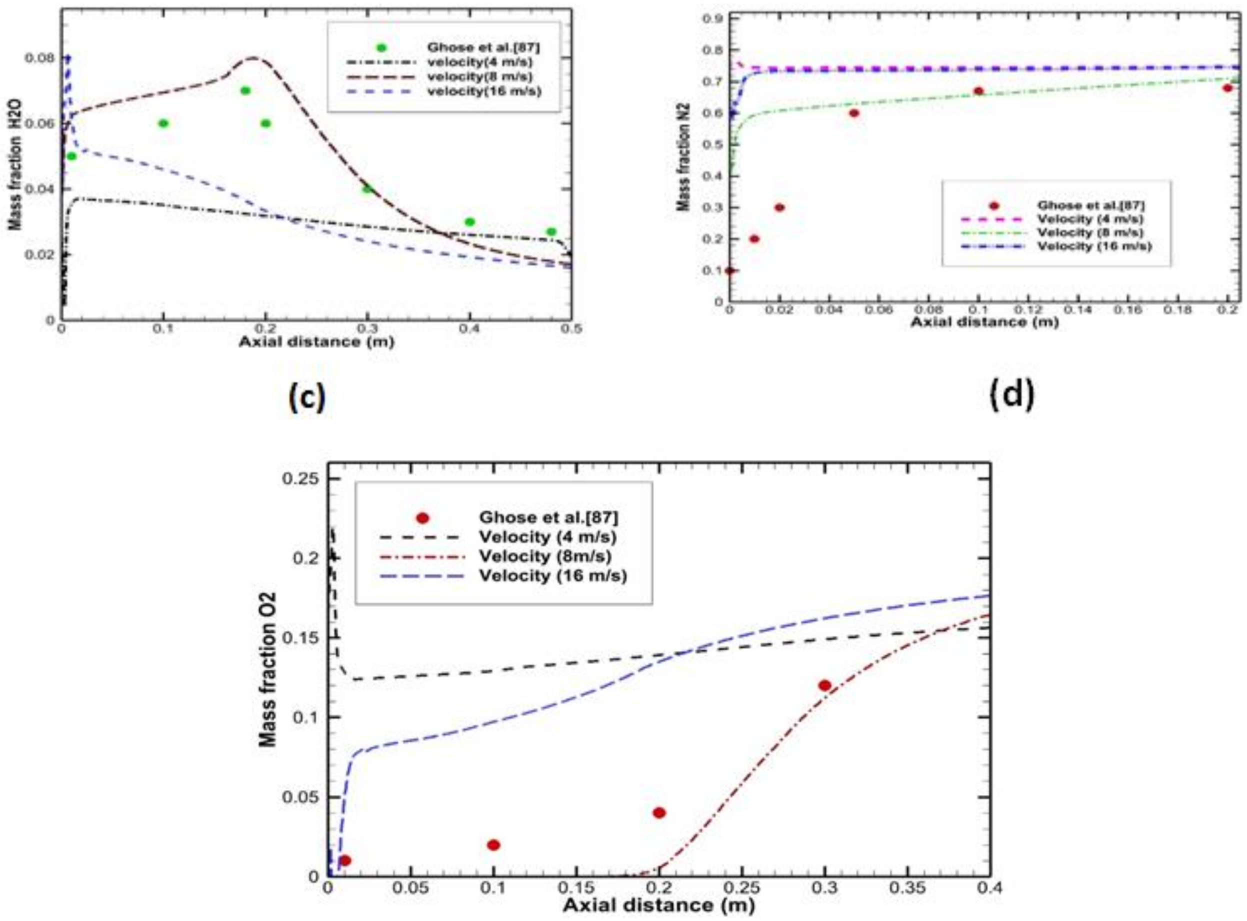

(c) (d)

(e)

Figure 7(a - e). Comparison between Ghose et al and Present work for Distribution of species mass fraction along the axis at 40° swirler vane angle and variable velocity (4, 8,16 m/s).

Figure 8. The fuel ($C_{12}H_{23}$) vapor in the velocity 8 m/s closer to Ghose et al case According to

1. Figure 8 (a), the mass fraction at the injector is 0.7. At about 0.001 m from the injector plane, the fuel vapor concentration rapidly to become less than 0.001 around 0.02 m, the fuel vapor concentration rapidly decreases around velocity 4 m/s and 16 m/s. The co2 mass fraction in the velocity 8 m/s closer to Ghose et al.

2. Figure 8 (b), the mass fraction at the injector is 0.05. At about 0.001 m from the injector plane, the co2 mass fraction concentration rapidly to become more than 0.19 around 0.1 m, the co2 mass fraction concentration velocity 4 m/s and 16 m/s increase 0.09 around 0.001m then decrease 0.05 around 0.5m. The H2O mass fraction in the velocity 8 m/s closer to Ghose et al case According to

3. Figure 8 (c), the mass fraction near injector is 0.05 about 0.001 m from the injector plane, the H2O mass fraction concentration to become less than 0.01 around 0. 5 m, the H2O mass fraction concentration decreases around velocity 4 m/s and 16 m/s. The N2 mass fraction in the velocity 8 m/s closer to Ghose et al.

4. Figure 8 (d), the mass fraction near injector is 0.28 about 0.001 m from the injector plane, the N2 mass fraction concentration to become increase to 0.7 around 0. 1 m, the N2 mass fraction concentration increases around velocity 4 m/s and 16 m/s. The O2 mass fraction in the velocity 8 m/s closer to Ghose et al.

5. Figure 8 (e), the mass fraction at the injector is 0.001 about 0.001 m from the injector plane, the O2 mass fraction concentration rapidly to become more than 0.1 around 0. 3 m, the O2 mass fraction concentration rapidly increases around velocity 4 m/s and 16 m/s.

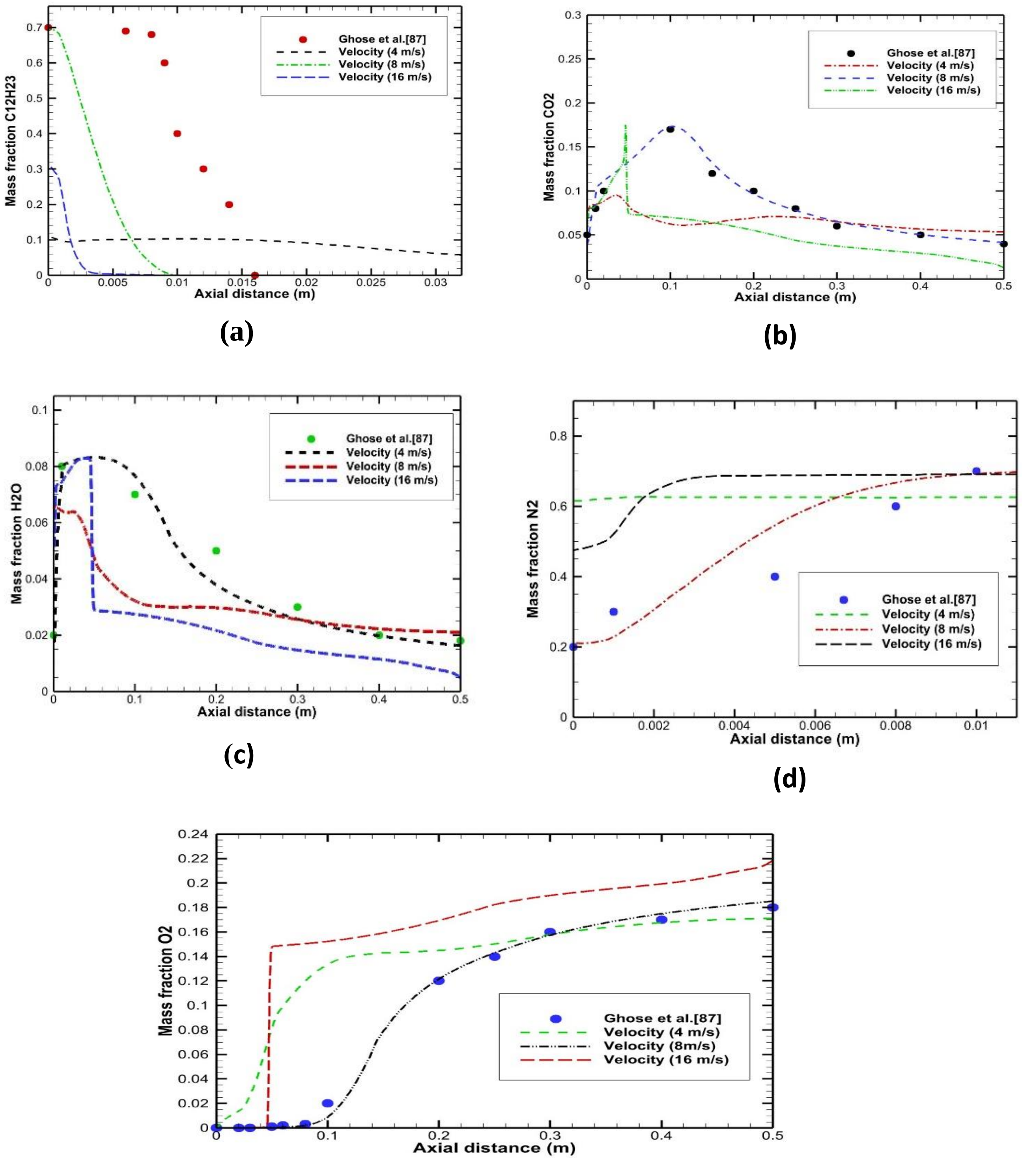

(a) **(b)** **(c)** **(d)** **(e)**

Figure 8 (a - e). Comparison between Ghose et al and Present work for Distribution of species mass fraction along the axis at 50° swirler vane angle and variable velocity (4, 8,16 m/s)

Figure 9. The fuel (C12H23) vapor in the velocity 8 m/s closer to Ghose et al case According to

1. Figure 9 (a), the mass fraction at the injector is 0.3 at about 0.001 m from the injector plane, the fuel vapor concentration rapidly to become less than 0.001 around 0.001 m, the fuel vapor concentration rapidly decreases around velocity 4 m/s, decreases at velocity 16 m/s. The co2 mass fraction in the velocity 8 m/s near to Ghose et al.

2. Figure 8 (b), the mass fraction at the injector is 0.06. At about 0.001 m from the injector plane, the co2 mass fraction concentration rapidly to become more than 0.17 around 0.025 m, the co2 mass fraction concentration velocity 4 m/s and 16 m/s decrease 0.03around 0.5m. The H2O mass fraction in the velocity 8 m/s closer to Ghose et al.

3. Figure 8 (c), the mass fraction near injector is 0.08 about 0.001 m from the injector plane, the H2O mass fraction concentration to become less than 0.02 around 0. 5 m, the H2O mass fraction concentration decreases around velocity 4 m/s and 16 m/s. The N2 mass fraction in the velocity 8 m/s closer to Ghose et al.

4. Figure 8 (d), the mass fraction near injector is 0.08 about 0.001 m from the injector plane, the N2 mass fraction concentration to become less than 0.7 around 0. 2 m, the N2 mass fraction concentration increases around velocity 4 m/s and 16 m/s. The O2 mass fraction in the velocity 8 m/s near to Ghose et al.

5. Figure 8 (e), the mass fraction at the injector is 0.001. At about 0.001 m from the injector plane, the O2 mass fraction concentration rapidly to become more than 0.19 around 0. 5 m, the O2 mass fraction concentration rapidly decreases around velocity 4 m/s but increases at 16 m/s.

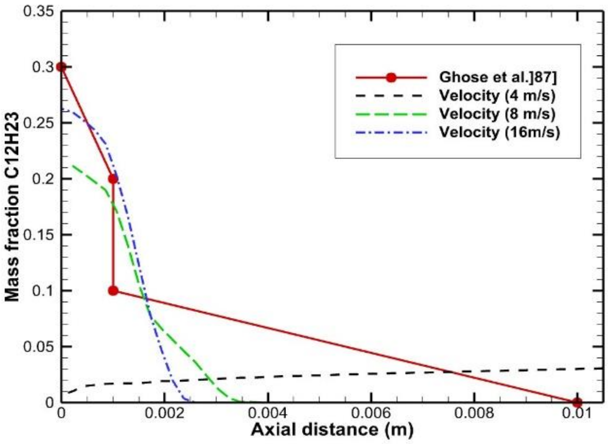

(a)

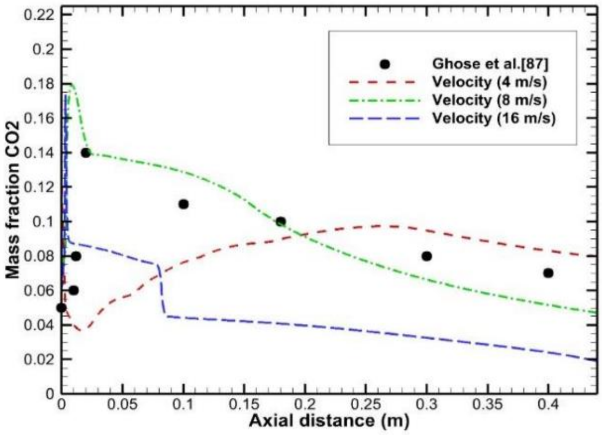

(b)

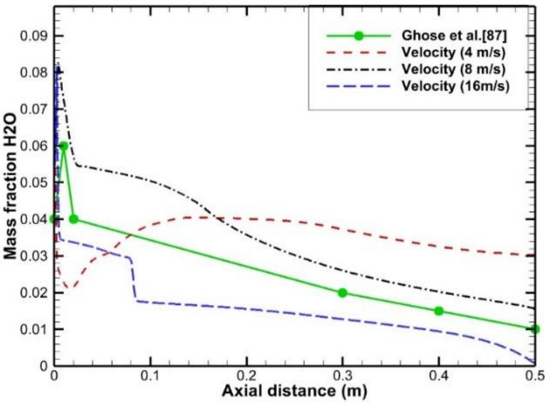

(c)

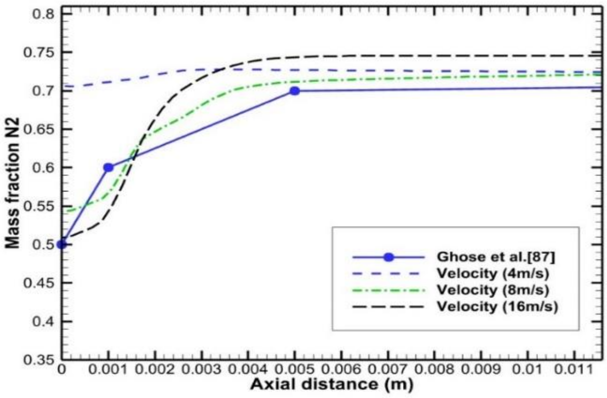

(d)

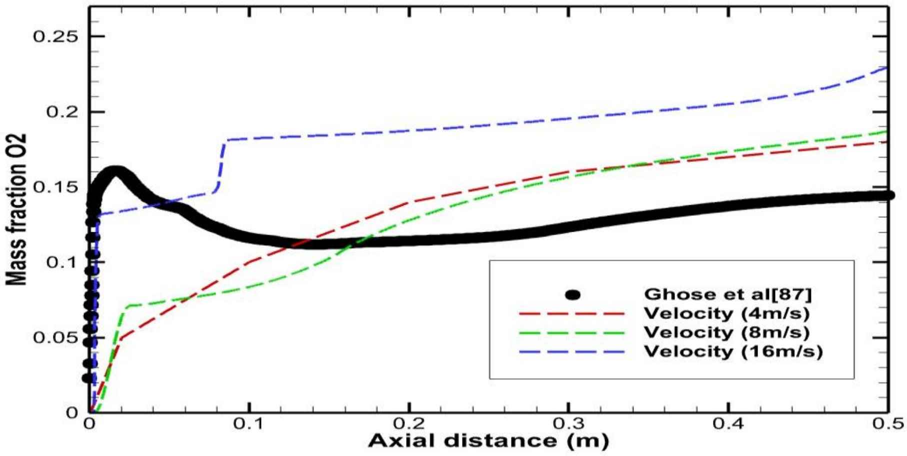

(e)

Figure 9 (a - e). Comparison between Ghose et al and Present work for Distribution of species mass fraction along the axis at 60° swirler vane angle and variable velocity (4, 8,16 m/s)

Turbulent kinetic energy distribution along the axis

1. Figure 10(a) shows a comparison between the turbulent kinetic energy of the gas phase along the centerline for various three swirler vane angle (40°, 50°, 60°), at velocity (4 m/s). During an interaction between liquid and gas phases, the turbulent kinetic energy about (50°) expresses a broad build-up of the turbulence field, which is distributed near the nozzle region. Where the value starts from 24 at 0.01m near the nozzle, then it gradually decreases until it reaches 3 at the distance 0.5m. The turbulent kinetic energy about (60°) produces the same induction but at the lower rate. While the turbulent kinetic energy about (40◦) is expressing difference behavior from them, it increases from zero to 12 m2/s2 around peak. then degreases at 2 around 0.5m.

2. Figure 10 (b). Shows a comparison between the turbulent kinetic energy of the gas phase along the centerline for various three swirler vane angle (40° , 50°, 60°), at velocity (8 m/s). During an interaction between liquid and gas phases, the turbulent kinetic energy about (40°) expresses a broad build-up of the turbulence field, which is distributed near the nozzle region. Where the value starts from 28 at 0.01m near the nozzle, then it gradually decreases until it reaches 2 at the distance 0.5m. The turbulent kinetic energy about (50◦) produces the same induction but at the lower rate. While the turbulent kinetic energy about (60◦) is expressing difference behavior from them.

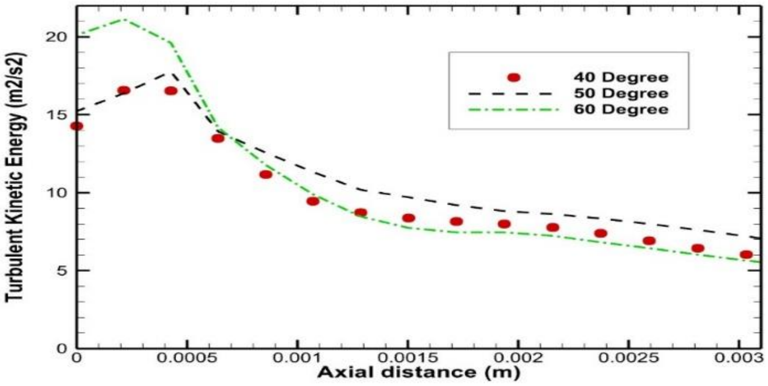

(a)

3. Figure 10(c) shows a comparison between the turbulent kinetic energy of the gas phase along the centerline for various three swirler vane angle (40◦ ,50◦, 60◦), at velocity (16 m/s). During an interaction between liquid and gas phases, the turbulent kinetic energy about (50◦) expresses a broad build-up of the turbulence field, which is distributed near the nozzle region. Where the value starts from 24 at 0.01m near the nozzle, then it gradually decreases until it reaches 3 at the distance 0.5m. The turbulent kinetic energy about (60◦) produces the same induction but at the lower rate. While the turbulent kinetic energy about (40◦) is expressing difference behavior from them, it increases from 5 to 20 m2/s2 around peak. then degreases at 2 around 0.5m.

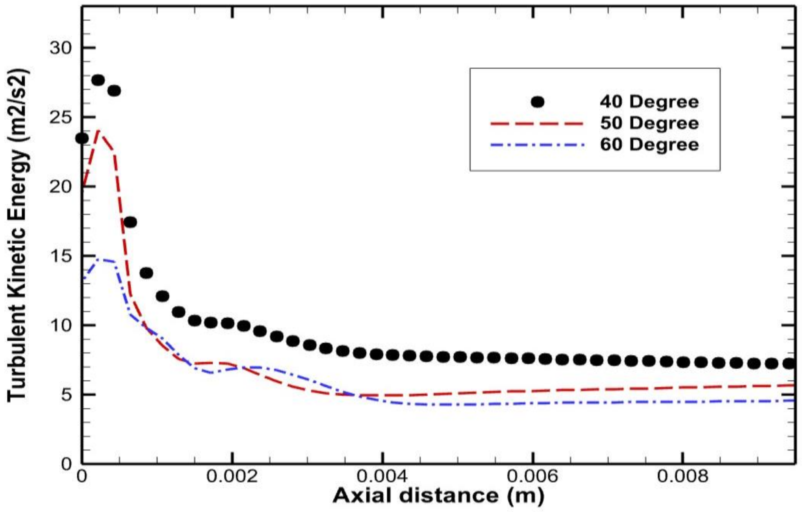

(b)

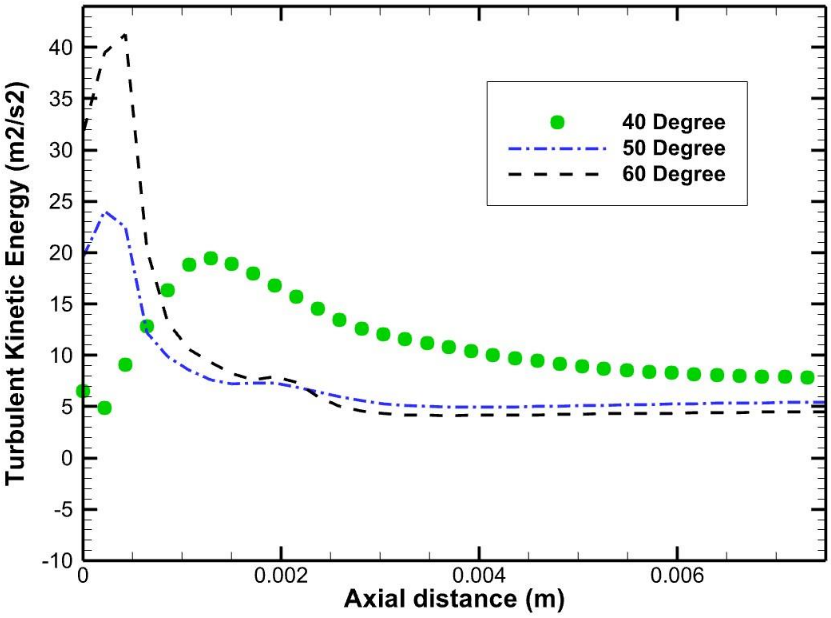

(c)

Figure 10 (a-c). Turbulent kinetic energy profile of the gas phase at different swirler vane angle the centerline at velocity (a- 4m/s, b- 8m/s, c- 16 m/s)

1. Figure 11(a) shows a comparison between the turbulent kinetic energy of the gas phase along the centerline for various three velocity (4m/s, 8m/s, 16m/s), at swirler vane angle (40◦). During

an interaction between liquid and gas phases, the turbulent kinetic energy about (8m/s) expresses a broad build-up of the turbulence field, which is distributed near the nozzle region. Where the value starts from 28 at 0.01m near the nozzle, then it gradually decreases until it reaches 2 at the distance 0.5m. The turbulent kinetic energy about (16m/s) produces the same induction but at the lower rate. While the turbulent kinetic energy about (4m/s) is expressing difference behavior from them, it increases from zero to 12 m2/s2 around peak. then degreases at 2 around 0.5m.

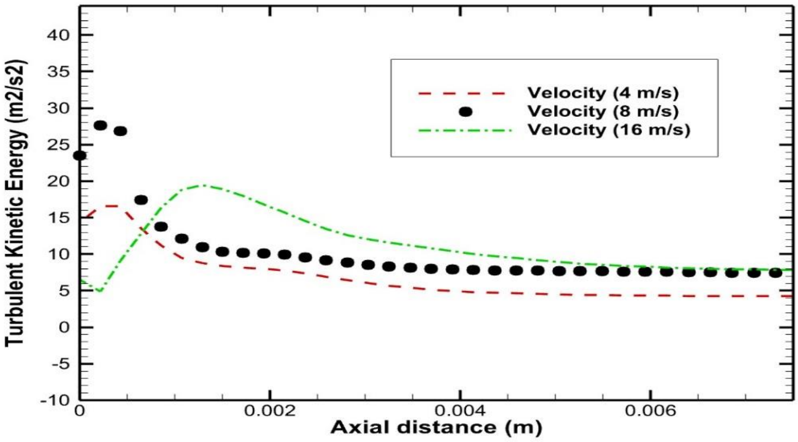

(a)

2. Figure 11(b) shows a comparison between the turbulent kinetic energy of the gas phase along the centerline for various three velocity (4m/s ,8m/s, 16m/s), at swirler vane angle (50◦). During an interaction between liquid and gas phases, the turbulent kinetic energy about (8m/s) expresses a broad build-up of the turbulence field, which is distributed near the nozzle region. Where the value starts from 28 at 0.01m near the nozzle, then it gradually decreases until it reaches 2 at the distance 0.5m. The turbulent kinetic energy about (16m/s) produces the same induction but at the lower rate. While the turbulent kinetic energy about (4m/s) is expressing difference behavior from them, it increases from zero to 12 m2/s2 around peak. then degreases at 2 around 0.5m.

3. Figure 11(c), shows a comparison between the turbulent kinetic energy of the gas phase along the centerline for various three velocity (4m/s ,8m/s, 16m/s), at swirler vane angle (60◦). During an interaction between liquid and gas phases, the turbulent kinetic energy about (8m/s) expresses a broad build-up of the turbulence field, which is distributed near the nozzle region.

.

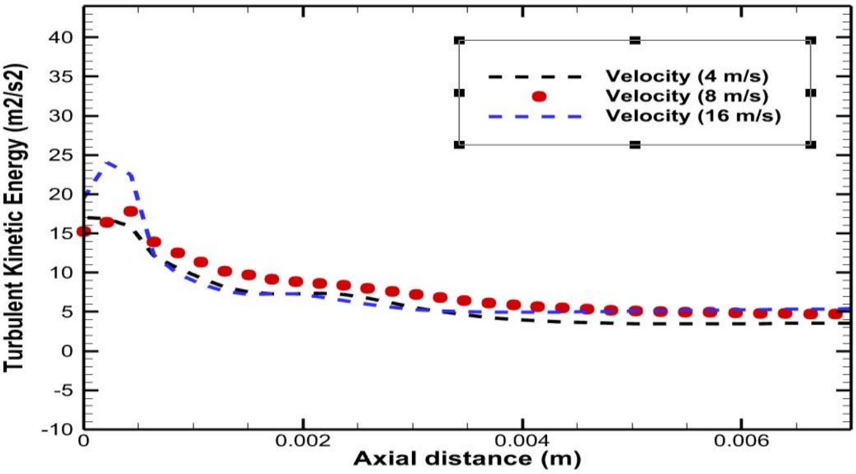

(b)

Where the value starts from 28 at 0.01m near the nozzle, then it gradually decreases until it reaches 2 at the distance 0.5m. The turbulent kinetic energy about (16m/s) produces the same induction but at the lower rate. While the turbulent kinetic energy about (4m/s) is expressing difference behavior from them, it increases from zero to 12 m2/s2 around peak. then degreases at 2 around 0.5m.

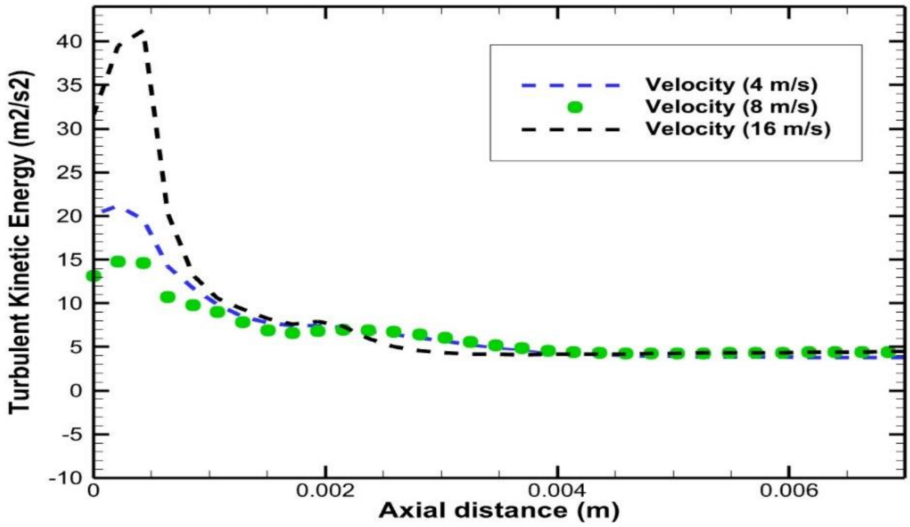

(c)

Figure 11. Turbulent kinetic energy profile of the gas phase at different velocity the centerline at swirler vane angle a- 40°, b-50°, b-60°

1. Figure 12(a), shows a comparison between the probability density function of the gas phase along the centerline for various three velocity (4m/s ,8m/s, 16m/s), at swirler vane angle (40◦). During an interaction between liquid and gas phases, the probability density function about (8m/s) expresses a broad build-up of the turbulence field, which is distributed closer the nozzle region. Where the value starts from 1.8 at 0.01m near the nozzle, then it gradually decreases until it reaches 0.001 at the distance 0.5m. The probability density function about (16m/s) value 0.19 at 0.001m then reduce to 0.02 at 0.03m produces the same induction but at the lower rate. While the probability density function about (4m/s) is expressing difference behavior from them, it increases from zero to 0.02 at 0.01m. then degreases at 0.01 around 0.5m.

2. Figure 12(b) shows a comparison between the probability density function of the gas phase along the centerline for various three velocity (4m/s ,8m/s, 16m/s), at swirler vane angle (40◦). During an interaction between liquid and gas phases, the probability density function about (8m/s) expresses a broad build-up of the turbulence field, which is distributed closer the nozzle region. Where the value starts from 5.5 at 0.001m near the nozzle, then it gradually decreases until it reaches 0.09 at the distance 0.001m, gradually decreases to 0.02 at 0.5m. The probability density function about (16m/s) value 0.38 at 0.001m then reduce to 0.02 at 0.05m produces the same induction but at the lower rate. While the probability density function about (4m/s) is expressing difference behavior from them, it increases from zero to 0.02 at 0.01m. then degreases at 0.01 around 0.5m.

3. Figure 12(c) shows a comparison between the probability density function of the gas phase along the centerline for various three velocity (4m/s ,8m/s, 16m/s), at swirler vane angle (40◦). During an interaction between liquid and gas phases, the proboles density faction about (8m/s) expresses a broad build-up of the turbulence field, which is distributed closer the nozzle region. Where the value starts from 0.15 at 0.01m near the nozzle, then it gradually decreases until it

reaches 0.02 at the distance 0.5m. The probability density function about (16m/s) value 0.34 at 0.01m then reduce to 0.01 at 0.1m produces the same induction but at the lower rate. While the probability density function about (4m/s) is expressing difference behavior from them, it decreases from 0.09 at 0.01m to at 0.01 around 0.5m.

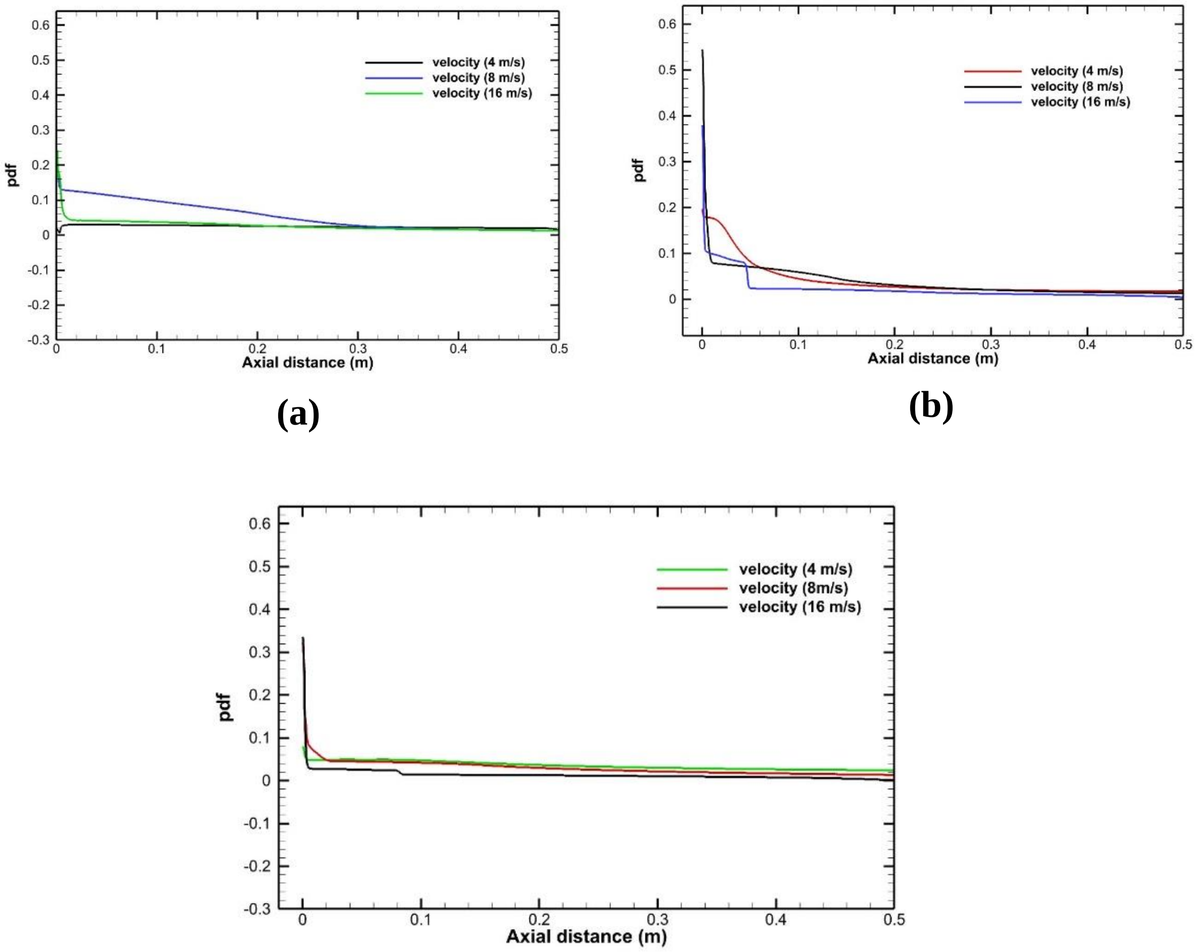

(a)

(b)

(c)

Figure 12. PDF profile of the gas phase at different swirler vane angle the centerline of a-40◦, b, 50◦ c-60◦

Conclusion

In this work, a numerical study has been performed to investigate the effects of inlet swirl and variation velocity on the spray combustion of kerosene issued from a pressure swirl atomizer in a cylindrical combustion chamber. Where the model parameters are suitably optimized for application in kerosene flames. The nucleation and surface growth model are to be significantly augmented from the to apply the model to kerosene flame. Radiative heat transfer from the flame has been considered, taking into account the contributions of participating gases. for simulating the radiation models for spray combustion of kerosene/air case, use various velocity (4m/s, 8m/s and 16m/s) the effects of input velocity on the spray combustion of kerosene emitted from a pressure swirl atomizer in a cylindrical combustion chamber were investigated numerically in this work. Where the model parameters are suitably optimized for application in kerosene flames., the nucleation and surface growth models must be greatly enhanced. Radiative heat transmission from the flame has been examined, with the contributions of participating gases taken into consideration.

Also, the effect of velocity on the gas temperature distribution. The factor affecting the exit pattern is analyzed. Combustors in different cases have been studied. It is found that increased swirl in the primary air flow shortens the flame. When the swirl is sufficiently strong, the flame even changes to an annular structure following a strong recirculation. Moreover, under a high swirl, the peak temperature in the flame decreases due to the mixing of excess air in the flame region. The species concentrations across the flame show that the flame length can be well mapped by the CO2 distribution in the combustor. Any combustion-related emissions by directing the peak radiative zone downstream along the combustor wall, a longer flame at a lower swirl increases the incident radiation heat flux on the wall's periphery. It is discovered that when the swirl increases, the temperature of the combustor wall rises, increasing heat loss and lowering combustor efficiency. On the other side, as the number of swirls grows, so does the incident radiation heat flux on the injector-swirler system. It is discovered that the injector is the more important component since its temperature is significantly higher than that of the swirler vanes. Because of the flame's proximity to the inlet plane, the injector's peak temperature rises as the swirl flow increases. However, when the swirl increases and the combustor's flow mixing is improved, the exhaust gas temperature distribution becomes more uniform. For various velocity situations, the temperature distributions on the combustor wall as well as the swirler-injector assembly have been compared and studied. The 8m/s velocity gives a better agreement with Ghose et al.

References

1. Lefebvre, A.H. and D.R. Ballal, *Gas turbine combustion: alternative fuels and emissions*. 2010: CRC press.
2. Koff, B.L., *Gas turbine technology evolution: a designers perspective.* Journal of propulsion and power, 2004. **20**(4): p. 577-595.
3. Arghode, V.K. and A.K. Gupta, *Development of high intensity CDC combustor for gas turbine engines.* Applied Energy, 2011. **88**(3): p. 963-973.
4. Düwel, I., et al., *Experimental and numerical characterization of a turbulent spray flame.* Proceedings of the Combustion Institute, 2007. **31**(2): p. 2247-2255.
5. Mikami, M., S. Miyamoto, and N. Kojima, *Counterflow diffusion flame with polydisperse sprays.* Proceedings of the Combustion Institute, 2002. **29**(1): p. 593-599.
6. Poorhoseinni, H., A. Saeedi, and M. Moghiman, *Experimental and numerical investigation of the inlet air swirl angle effects on temperature profile and CO, NO pollutants.* Energy Engineering & Management, 2012. **2**(1): p. 32-39.
7. Zhou, Y., et al., *An improved model to calculate radiative heat transfer in hot combustion gases.* Combustion Theory and Modelling, 2020. **24**(5): p. 829-851.
8. Zhou, H. and S. Meng, *Numerical prediction of swirl burner geometry effects on NOx emission and combustion instability in heavy oil-fired boiler.* Applied Thermal Engineering, 2019. **159**: p. 113843.
9. Bonatesta, F., et al. *The influence of swirl ratio on soot quantity and distribution in the cylinder of a diesel engine.* in *Third European Combustion Meeting ECM*. 2007.
10. Roberts, H.C., et al., *A review of the measurement of grip strength in clinical and epidemiological studies: towards a standardised approach.* Age and ageing, 2011. **40**(4): p. 423-429.

11. Patel, V. and R. Shah, *Effect of swirl and number of swirler vanes on combustion characteristics of methane inverse diffusion flame.* Journal of Mechanical Science and technology, 2019. **33**: p. 1947-1958.
12. Khelil, A., et al., *Prediction of a high swirled natural gas diffusion flame using a PDF model.* Fuel, 2009. **88**(2): p. 374-381.
13. Khanafer, K. and S. Aithal, *Fluid-dynamic and NOx computation in swirl burners.* International Journal of Heat and Mass Transfer, 2011. **54**(23-24): p. 5030-5038.
14. Sloman, A., *What ue lhe llbas of Science?*
15. Jones, W., A. Marquis, and K. Vogiatzaki, *Large-eddy simulation of spray combustion in a gas turbine combustor*. Combustion and Flame, 2014. **161**(1): p. 222-239.
16. Yılmaz, I., *Effect of swirl number on combustion characteristics in a natural gas diffusion flame*. Journal of Energy Resources Technology, 2013. **135**(4).
17. Hosseini, A.A., et al., *Numerical study of inlet air swirl intensity effect of a Methane-Air Diffusion Flame on its combustion characteristics.* Case Studies in Thermal Engineering, 2020. **18**: p. 100610.
18. Datta, A. and S. Som, *Combustion and emission characteristics in a gas turbine combustor at different pressure and swirl conditions.* Applied Thermal Engineering, 1999. **19**(9): p. 949-967.
19. Rohani, B. and K.M. Saqr, *Effects of hydrogen addition on the structure and pollutant emissions of a turbulent unconfined swirling flame.* International Communications in Heat and Mass Transfer, 2012. **39**(5): p. 681-688.
20. Ko, J., et al., *Chemically resistant and thermally stable quantum dots prepared by shell encapsulation with cross-linkable block copolymer ligands.* NPG Asia Materials, 2020. **12**(1): p. 1-11.
21. Choi, C.E. and S.W. BAEK, *Numerical analysis of a spray combustion with nongray radiation using weighted sum of gray gases model.* Combustion science and technology, 1996. **115**(4-6): p. 297-315.
22. Pope, S., *Combustion Modelling using Probability Density Function Methods.* Numerical Approaches to Combustion Modelling, Prog. Astronaut. Aeronaut, AIAA, 1991.
23. Morsi, S. and A. Alexander, *An investigation of particle trajectories in two-phase flow systems.* Journal of Fluid mechanics, 1972. **55**(2): p. 193-208.
24. Chui, E. and G. Raithby, *Computation of radiant heat transfer on a nonorthogonal mesh using the finite-volume method.* Numerical Heat Transfer, 1993. **23**(3): p. 269-288.
25. Raithby, G. and E. Chui, *A finite-volume method for predicting a radiant heat transfer in enclosures with participating media.* 1990.
26. Ghose, P., et al., *Prediction of soot and thermal radiation in a model gas turbine combustor burning kerosene fuel spray at different swirl levels.* Combustion Theory and Modelling, 2016. **20**(3): p. 457-485.